Journal of Advanced Ceramics
2021, **10**(2): 377–384
https://doi.org/10.1007/s40145-021-0462-5
ISSN 2226-4108
CN 10-1154/TQ

Rapid Communication

Electrical and thermal transport behaviours of high-entropy perovskite thermoelectric oxides

Yunpeng ZHENG[a], Mingchu ZOU[a], Wenyu ZHANG[a], Di YI[a], Jinle LAN[b], Ce-Wen NAN[a], Yuan-Hua LIN[a,*]

[a]*State Key Laboratory of New Ceramics and Fine Processing, School of Materials Science and Engineering, Tsinghua University, Beijing 100084, China*
[b]*State Key Laboratory of Organic-Inorganic Composites, Beijing University of Chemical Technology, Beijing 100029, China*

Received: January 15, 2021; Accepted: January 21, 2021

Abstract: Oxide-based ceramics could be promising thermoelectric materials because of their thermal and chemical stability at high temperature. However, their mediocre electrical conductivity or high thermal conductivity is still a challenge for the use in commercial devices. Here, we report significantly suppressed thermal conductivity in $SrTiO_3$-based thermoelectric ceramics via high-entropy strategy for the first time, and optimized electrical conductivity by defect engineering. In high-entropy $(Ca_{0.2}Sr_{0.2}Ba_{0.2}Pb_{0.2}La_{0.2})TiO_3$ bulks, the minimum thermal conductivity can be 1.17 W/(m·K) at 923 K, which should be ascribed to the large lattice distortion and the huge mass fluctuation effect. The power factor can reach about 295 μW/(m·K^2) by inducing oxygen vacancies. Finally, the *ZT* value of 0.2 can be realized at 873 K in this bulk sample. This approach proposed a new concept of high entropy into thermoelectric oxides, which could be generalized for designing high-performance thermoelectric oxides with low thermal conductivity.

Keywords: high entropy; thermoelectric oxides; thermal conductivity; electrical conductivity; oxygen vacancy

1 Introduction

Thermoelectric materials could realize direct heat–electricity conversion without the use of mechanical devices which limit miniaturization of energy conversion products [1,2]. The dimensionless figure of merit, $ZT = \sigma S^2 T / \kappa$, is used to evaluate the efficiency of thermoelectrics, where σ, S, T, κ are the electrical conductivity, Seebeck coefficient, temperature, and thermal conductivity, respectively.

Thermoelectric oxides, including simple oxides ZnO [3,4], TiO_2 [5], In_2O_3 [6], layered oxides BiCuSeO [7,8], Bi_2O_2Se [9], $NaCo_2O_4$ [10], $Ca_3Co_4O_9$ [11], $Bi_2Sr_2Co_2O_y$ [12], and perovskite oxides $SrTiO_3$ [13], $CaMnO_3$ [14], etc., are a promising material family for thermoelectric applications due to their thermal stability, chemical stability, and low cost. Among all the thermoelectric oxides, perovskite titanate ($ATiO_3$) like $SrTiO_3$-based thermoelectrics, attract much attention because of their high symmetry structure which leads to high degeneracy, high effective mass, and consequently

* Corresponding author.
E-mail: linyh@tsinghua.edu.cn

high Seebeck coefficient. However, the high lattice thermal conductivity caused by strong metal–oxygen ion bonds limits the enhancement of *ZT* of thermoelectric oxides. Generally, minimizing lattice thermal conductivity could significantly improve *ZT* of thermoelectric oxides [15]. Normally, the strategies including point defect scattering [16], nano-scale modulation [17], and composite effects [18–20] were applied to reduce the lattice thermal conductivity of $SrTiO_3$-based thermoelectrics. However, the lattice thermal conductivity remains above 2 W/(m·K) even at relatively high temperature. More effective strategies are needed to further suppress the thermal conductivity of perovskite thermoelectric oxides.

High-entropy ceramics have been widely studied since they were successfully synthesized by Rost *et al.* [21] in 2015. The concept of high-entropy ceramics was introduced from the field of high-entropy alloys, and similarly, when the configurational entropy $\Delta S_{\text{mix}} > 1.5R$, the ceramics could be categorized as high-entropy ceramics [22]. When there is only one site occupied by different elements, at least five elements of equivalent molar fraction are needed to satisfy the criteria of 1.5*R*. High-entropy ceramics could be potential for high-performance thermoelectrics, considering the following points. Solid solution is stabilized in high-entropy ceramics, which provides more opportunities of element tuning and heavy doping [23]. The large lattice distortion and the huge mass fluctuation in high-entropy ceramics result in significantly suppressed lattice thermal conductivity [24,25]. High symmetry phase tends to form when the entropy is high enough, which makes the improvement of band degeneracy and Seebeck coefficient possible.

In this work, pure perovskite phase A-site high-entropy thermoelectric oxide $(Ca_{0.2}Sr_{0.2}Ba_{0.2}Pb_{0.2}La_{0.2})TiO_3$ ($\Delta S_{\text{mix}} \approx 1.609R$) was synthesized by solid state reaction and conventional sintering. Our results indicate that the high-entropy strategy at A-site with equivalently added five elements (Ca, Sr, Ba, Pb, La) greatly suppressed the lattice thermal conductivity to 1.09 W/(m·K) at 923 K. After being annealed under electrical current in reducing atmosphere to create oxygen vacancies in the bulk, the high-entropy oxides displayed a maximum power factor of ~295 μW/(m·K^2). *ZT* of over 0.2 at 873 K was realized in the sample annealed at 0.2 A/mm^2. This work paves a new path to reducing the thermal conductivity in thermoelectric oxides.

2 Materials and methods

Polycrystalline high-entropy perovskite oxides $(Ca_{0.2}Sr_{0.2}Ba_{0.2}Pb_{0.2}La_{0.2})TiO_3$ were prepared by solid state reaction and conventional sintering. Molar fraction of 20% $CaTiO_3$, 20% $SrTiO_3$, 20% $BaTiO_3$, 21% $PbTiO_3$ (5% excess, considering the volatilization characteristic of $PbTiO_3$), 10% La_2O_3, 19% TiO_2 were mixed by planetary ball milling using ethanol as milling agent. After the mixed powder was dried, the powder was pressed into pellets of 20 mm in diameter under a pressure of 40 MPa for 3 min. The mechanically shaped pellets were then pressed under a pressure of ~200 MPa in the cold isostatic pressing system. The pellets reacted and were sintered under 1200 ℃ for 50 h, buried in the raw mixed powder for protection. The as-prepared pellets (denoted as HEPO-E0) were sectioned into bars, and then the bars were annealed in 5%H_2–95%Ar mixed gas at 1000 ℃ for 1 h, with electrical current applied whose current densitie were 0.1, 0.2, 0.3, and 0.4 A/mm^2 (denoted as HEPO-E1, HEPO-E2, HEPO-E3, and HEPO-E4, respectively).

The bulk X-ray diffraction (XRD) data were collected by a D/max-2500 diffraction instrument (Rigaku, Japan, Cu Kα) with a scanning rate of 8 (°)/min. The sectional morphology and elemental distribution were observed by field-emission scanning electron microscopy (SEM, MERLIN VP Compact, ZEISS, Germany) with energy dispersion spectrometer (EDS) apparatus. The X-ray photoelectron spectroscopy (XPS) analysis was conducted on an X-ray photoelectron spectrometer (Thermo Fisher ESCALAB 250Xi, Al Kα). The electrical conductivity and the Seebeck coefficient were measured on ZEM-3 (ULVAC-RICO, Inc., Japan) from room temperature to 923 K in He gas. The thermal diffusivity measurements were carried out on LFA457 (NETZSCH LFA457 Micro Flash, Germany) with Ar as the purging gas, and the density data were acquired by Archimedes' method.

3 Results and discussion

To check the phase formation and crystallization process, XRD was performed on HEPO-E0, HEPO-E1, HEPO-E2, HEPO-E3, and HEPO-E4 (Fig. 1). Figure 1 shows that the as-prepared sample HEPO-E0 formed into a high-entropy cubic perovskite phase ($Pm\bar{3}m$) disordered solid solution with no other detectable

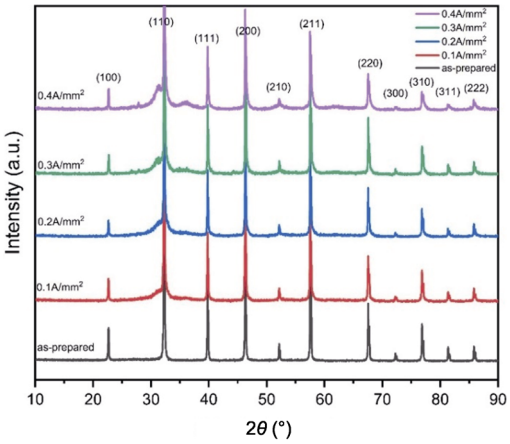

Fig. 1 XRD patterns of $(Ca_{0.2}Sr_{0.2}Ba_{0.2}Pb_{0.2}La_{0.2})TiO_3$ high-entropy perovskite oxides under the annealing treatment of different electrical current densities.

undesired peaks. There was a left shift of the peaks of the as-prepared sample, compared with the peaks of the cubic perovskite $CaTiO_3$ (PDF#43-0226) and $SrTiO_3$ (PDF#35-0734). The lattice parameter, *a*, was calculated, and the value was 3.916 Å, which means that the larger atoms of Ba, Pb, and La occupied A-site of the perovskite, leading to the expansion of the lattice. The pure sharp peaks indicate that the high temperature solid state reaction and conventional sintering for 50 h provided enough time for atomic diffusion, hence the formation of high symmetry perovskite phase disordered solid solution and the growth of crystal grains, though the diffusion coefficient of high-entropy ceramics was relatively low owing to the sluggish diffusion effect [26] and the lattice distortion effect in high-entropy materials [27,28].

It can be seen in the SEM images (Fig. 2) that, with enough time to grow, the grains of HEPO-E0 were around 1 μm in size. Comparing the SEM image of HEPO-E0 with that of HEPO-E4, it can be reckoned that the samples underwent grain growth and densification process when being annealed with electrical current applied, the reason for which may be that the externally applied electricity added to the energy for the atomic diffusion and the grain boundary migration. The EDS mappings in Fig. 3 show the uniform distribution of the elements in the high-entropy oxides. There were no obvious segregations or precipitations detected in EDS mappings, consistent with the conclusion drawn by XRD patterns. After the reducing process, as can be seen in Fig. 3(b), the elemental distribution stayed uniform, indicating that the creation of oxygen vacancies had little influence on the distribution of other elements at other sites. Combined with XRD patterns, high-entropy, pure perovskite-type, highly disordered solid solution, $(Ca_{0.2}Sr_{0.2}Ba_{0.2}Pb_{0.2}La_{0.2})TiO_3$ ceramics were realized by solid state reaction and conventional sintering, and maintained their uniform distribution and crystal structure after being annealed with external electrical current applied.

To understand the effect of electrical current assisted annealing on oxygen vacancies, the XPS measurements were performed. The Lorentzian–Gaussian fitting was applied to fit the multi-peak XPS curves, and the results are shown in Fig. 4. The three fitting peaks of O 1s (Fig. 4(a)) were peaks of lattice oxygen (O_l), deficient oxygen (O_d), and absorbed oxygen (O_a) from the low binding energy to the high binding energy [29]. After being reduced at the electrical current density of 0.4 A/mm^2, the intensity of the peak of O_d slightly increased, meaning that oxygen vacancies were created. We also revealed that the Ti^{4+}-to-Ti^{3+} transition was promoted after the reducing process. The valence of Ti ions was determined by XPS of Ti 2p peaks. The Ti^{3+} peaks located at around 457.5 and 462.9 eV, and the Ti^{4+} peaks located at 458.0 and 463.9 eV [20]. The percentage of Ti^{3+} was calculated by integrating the area of the relative peaks, and the molar fraction of Ti^{3+} increased from 20.4% to 33.6% in HEPO-E4. It can be inferred that the electrical current assisted reducing

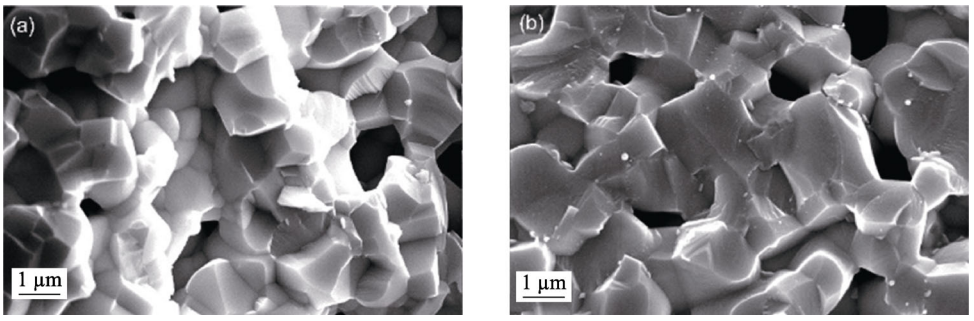

Fig. 2 SEM images of the sectional morphology of (a) HEPO-E0 and (b) HEPO-E4.

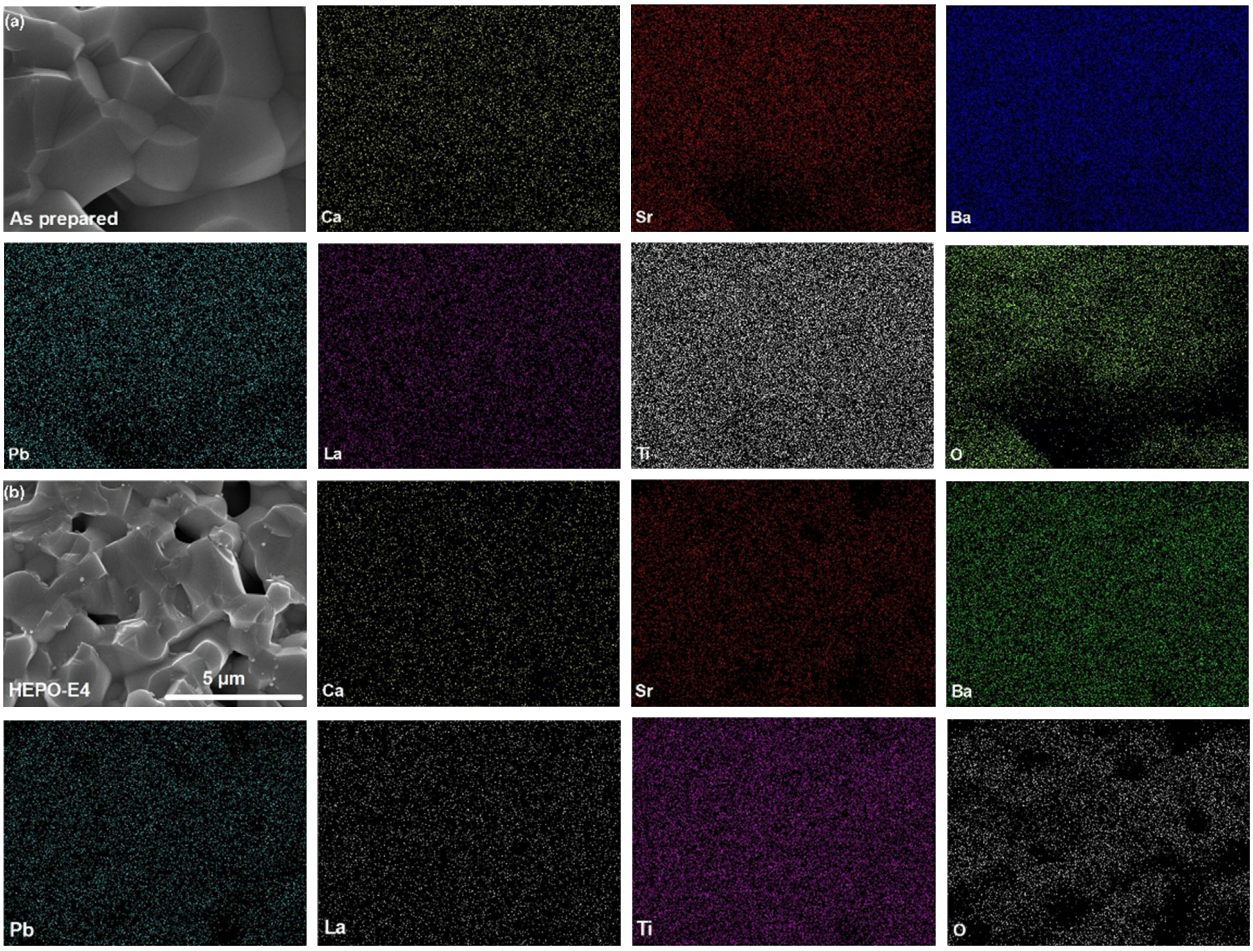

Fig. 3 EDS mappings on the sectional surface of (a) HEPO-E0 and (b) HEPO-E4.

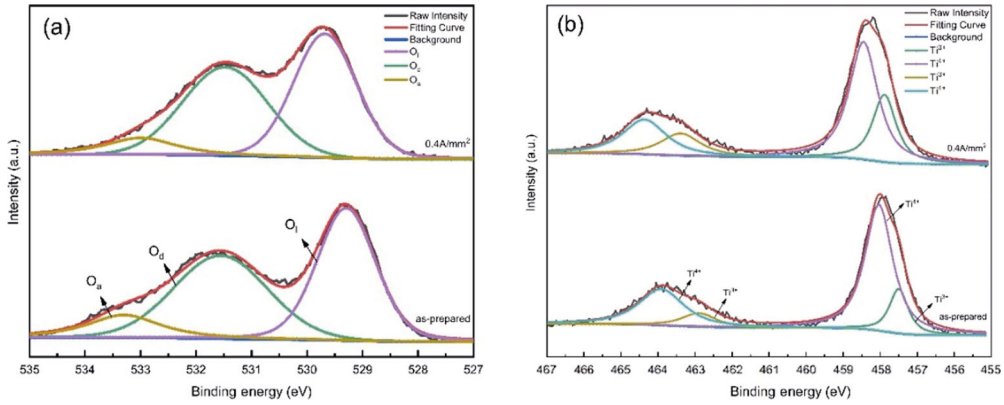

Fig. 4 XPS fittings for (a) oxygen and (b) titanium of HEPO-E0 and HEPO-E4.

annealing could promote the creation of Ti^{3+}, that is to say, the increase of the electron concentration. The corresponding reaction might be written as Eq. (1):

$$2Ti_{Ti} + O_O \rightarrow 2Ti'_{Ti} + V_O^{\bullet\bullet} + \frac{1}{2}O_2 \uparrow \quad (1)$$

When annealing the samples, the oxygen vacancies were activated by the reducing gas, 5%H_2–95%Ar. The electrical current "carried" the oxygen vacancies from one side to the other with the help of high temperature to improve the diffusivity of oxygen, and the lattice oxygen formed into oxygen gas at the cathode side of the external power. The "run-away" of oxygen vacancies boosted the reaction (Eq. (5)) forwards, and increasing number of Ti^{3+} were created. It was

important to mention that the electrical current assisted reducing was a bulk effect, other than the surface effect of simply annealing bulks in reducing gas because of the low diffusion coefficient of high-entropy ceramics and the long diffusion path of thick bulks.

Due to the large lattice distortion and the huge mass fluctuation of high-entropy perovskite oxides, the thermal diffusivity and the thermal conductivity were relatively low among $SrTiO_3$-based counterparts. As can be seen in Figs. 5(b) and 5(c), the total thermal conductivity and the lattice thermal conductivity of pure $SrTiO_3$ were relatively high, which were 9.79–5.56 W/(m·K) in the temperature range of 323–873 K [30]. When being doped by 10% La and 10% Nb [17], the thermal conductivity of $(Sr_{0.9}La_{0.1})(Ti_{0.9}Nb_{0.1})O_3$ was suppressed. However, its total thermal conductivity and lattice thermal conductivity were still over 2.9 and 2.3 W/(m·K) at 873 K, respectively. Meanwhile, the thermal conductivity was between 1.7 and 1.0 W/(m·K) for high-entropy $(Ca_{0.2}Sr_{0.2}Ba_{0.2}Pb_{0.2}La_{0.2})TiO_3$ perovskite oxides, outperforming the reference materials remarkably.

Generally, thermal conductivity is strongly correlated to the mass and strain fluctuations (described by disorder scattering factors Γ_{MF} and Γ_{SF}, respectively) and phonon relaxation time τ can be described by the following Eqs. (2)–(5) [31]. The phonon relaxation time and the thermal conductivity would decrease when the fluctuations of mass and strain increased.

$$\tau_D^{-1} = A\omega^4 = \frac{V}{4\pi v^3}\Gamma\omega^4 \tag{2}$$

$$\Gamma = \Gamma_{MF} + \Gamma_{SF} + \ldots \tag{3}$$

$$\Gamma_{MF} = \frac{\sum_{i=1}^{n} c_i \left(\frac{\bar{M}_i}{\bar{M}}\right)^2 f_i^1 f_i^2 \left(\frac{M_i^1 - M_i^2}{\bar{M}_i}\right)^2}{\sum_{i=1}^{n} c_i} \tag{4}$$

$$\Gamma_{SF} = \frac{\sum_{i=1}^{n} c_i \left(\frac{\bar{M}_i}{\bar{M}}\right)^2 f_i^1 f_i^2 \epsilon_i \left(\frac{r_i^1 - r_i^2}{\bar{r}_i}\right)^2}{\sum_{i=1}^{n} c_i} \tag{5}$$

The highly disordered high-entropy ceramics had large lattice distortion and huge mass difference at crystal sites, which made them promising materials with low thermal conductivity. Oxygen vacancies also played important role on thermal conductivity. When oxygen vacancies formed, they acted as defects to scatter short-wavelength phonons, and at the same time they added to the entropy at the oxygen site. The resultant effect was that the annealed samples all showed lower thermal diffusivity than those of the as-prepared sample. Additionally, the thermal conductivity differed slightly under various treatment conditions, which could be ascribed to the fact that the contribution of oxygen vacancies to phonon scattering might remain constant when annealing the samples.

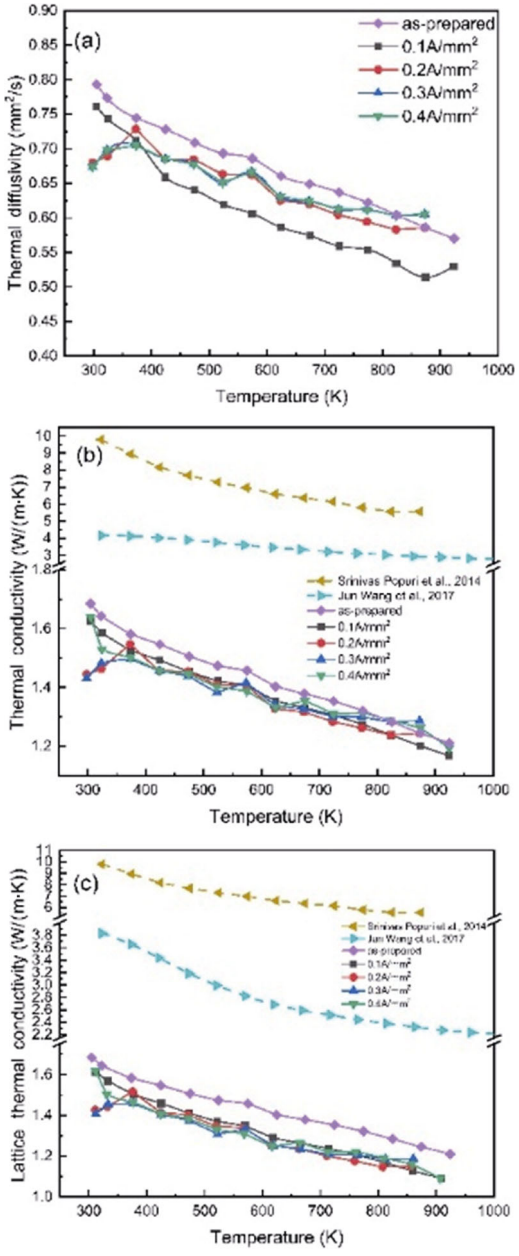

Fig. 5 Thermal properties of samples: (a) thermal diffusivity; (b) total thermal conductivity; (c) lattice thermal conductivity. The thermal conductivity as reference: pure $SrTiO_3$ [31]; 10%La–10%Nb co-doped $(Sr_{0.9}La_{0.1})(Nb_{0.1}Ti_{0.9})O_3$ [17].

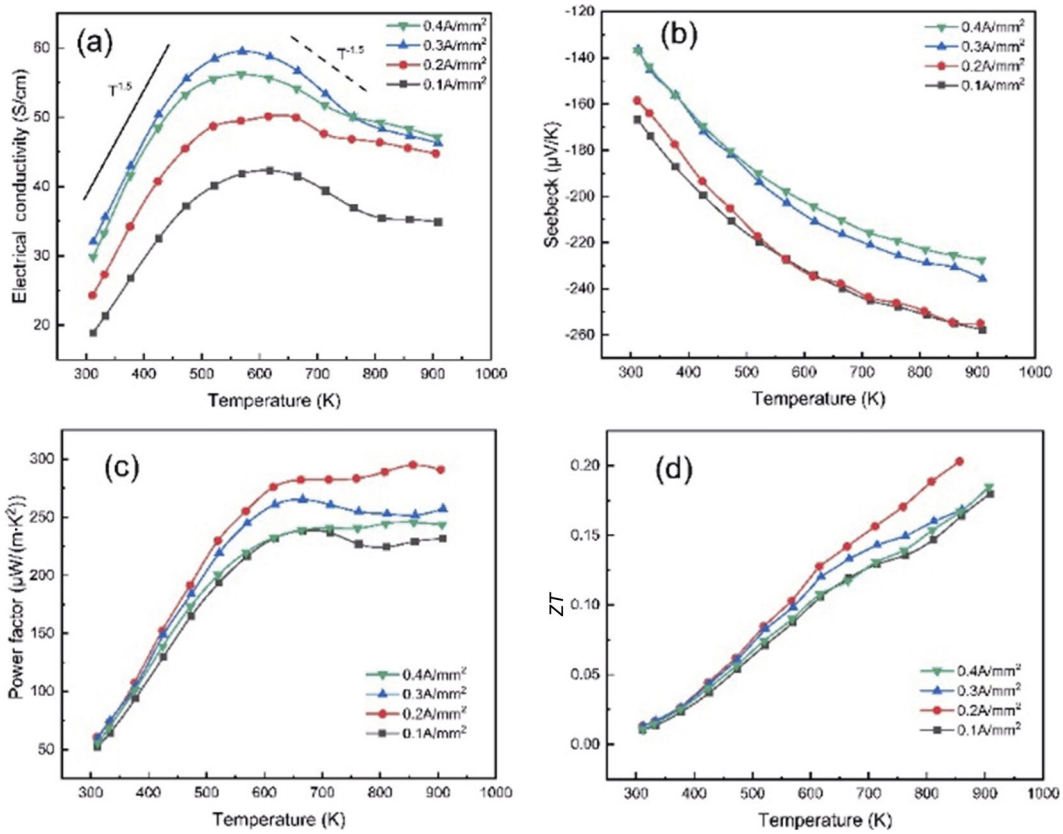

Fig. 6 Electrical properties and *ZT* of annealed $(Ca_{0.2}Sr_{0.2}Ba_{0.2}Pb_{0.2}La_{0.2})TiO_3$: (a) electrical conductivity; (b) Seebeck coefficient; (c) power factor; (d) *ZT*.

Our electrical measurements indicate that HEPO-E0 sample was insulated. The reduced bulk samples became conductive due to the induced oxygen vacancies. The carrier concentration can be enhanced from 8.88×10^{19} to 3.65×10^{20} cm^{-3} with increasing electrical current density from 0.1 to 0.4 A/mm^2. On the whole, the electrical conductivity of samples increased with increasing electron concentration, and the maximum electrical conductivity of ~60 S/cm was realized in HEPO-E3 sample at 573 K. At low temperature, the electrical conductivity–temperature relationship obeyed the $T^{1.5}$ rule caused by ionized impurity scattering [14], and at high temperature, the electrical conductivity was proportional to $T^{-1.5}$, which was typical of acoustic phonon scattering [32]. The absolute value of Seebeck coefficient decreased with increasing carrier concentration in Fig. 6(b), which can be explained by Eq. (6) [33]:

$$S=\frac{8\pi^2k_B^2}{3eh^2}m^*T\left(\frac{\pi}{3n}\right)^{\frac{2}{3}} \quad (6)$$

The Seebeck coefficient reached –250 μV/K in HEPO-E1 and HEPO-E2 at 923 K. For the Ti-site element remained undisturbed, the electrical performance was similar to other perovskite titanates. The *PF* remained constant at high temperature for all annealed samples, and the highest *PF* ~295 $\mu W/(m\cdot K^2)$ was observed in HEPO-E2 sample. The maximum *ZT* of over 0.2 at 873 K was also realized in this sample.

4 Conclusions

In summary, high-entropy $(Ca_{0.2}Sr_{0.2}Ba_{0.2}Pb_{0.2}La_{0.2})TiO_3$ ceramics have been successfully synthesized by solid state reaction and electrical current assisted reducing process. Our results show that the lattice thermal conductivity can be reduced from 5.56 W/(m·K) of pure $SrTiO_3$ to 1.09 W/(m·K) of $(Ca_{0.2}Sr_{0.2}Ba_{0.2}Pb_{0.2}La_{0.2})TiO_3$ at 873 K due to the large lattice distortion and the mass fluctuation effect. High carrier concentration can be realized by the generated large amount of oxygen vacancies from the Ti^{4+}-to-Ti^{3+} transition under the electrical current treatments. The oxygen vacancies were also effective to scatter short-wavelength phonons and further lower the lattice thermal conductivity. The *ZT* of over 0.2 was achieved in the sample annealed at the

current density of 0.2 A/mm^2. The concept of high-entropy thermoelectric oxides may provide new possibility to realize advanced thermoelectrics with low thermal conductivity.

Acknowledgements

We thank Yu Xiao from Beihang University for samples' thermal conductivity measurements. This work was financially supported by Basic Science Center Project of the National Natural Science Foundation of China under Grant No. 51788104, National Key Research Program of China under Grant No. 2016YFA0201003, and the National Natural Science Foundation of China under Grant No. 51729201.

References

[1] Nielsch K, Bachmann J, Kimling J, *et al*. Thermoelectric nanostructures: From physical model systems towards nanograined composites. *Adv Energy Mater* 2011, **1**: 713–731.

[2] Pei YZ, Zhou XY, Zhu TJ. Editorial for rare metals, special issue on advanced thermoelectric materials. *Rare Met* 2018, **37**: 257–258.

[3] Zhou ZF, Ren GK, Tan X, *et al*. Enhancing the thermoelectric performance of ZnO epitaxial films by Ga doping and thermal tuning. *J Mater Chem A* 2018, **6**: 24128–24135.

[4] Cai KF, Müller E, Drašar C, *et al*. Preparation and thermoelectric properties of Al-doped ZnO ceramics. *Mat Sci Eng B* 2003, **104**: 45–48.

[5] Baumard JF, Tani E. Thermoelectric power in reduced pure and Nb-doped TiO_2 rutile at high temperature. *Phys Status Solidi a* 1977, **39**: 373–382.

[6] Ohtaki M, Ogura D, Eguchi K, *et al*. High-temperature thermoelectric properties of In_2O_3-based mixed oxides and their applicability to thermoelectric power generation. *J Mater Chem* 1994, **4**: 653.

[7] Zhao LD, Berardan D, Pei YL, *et al*. $Bi_{1-x}Sr_xCuSeO$ oxyselenides as promising thermoelectric materials. *Appl Phys Lett* 2010, **97**: 092118.

[8] Liu R, Tan X, Liu YC, *et al*. BiCuSeO as state-of-the-art thermoelectric materials for energy conversion: From thin films to bulks. *Rare Metal* 2018, **37**: 259–273.

[9] Liu R, Lan JL, Tan X, *et al*. Carrier concentration optimization for thermoelectric performance enhancement in n-type Bi_2O_2Se. *J Eur Ceram Soc* 2018, **38**: 2742–2746.

[10] Ito M, Furumoto D. Effects of noble metal addition on microstructure and thermoelectric properties of Na_xCo_2O4. *J Alloys Compd* 2008, **450**: 494–498.

[11] Wang Y, Sui Y, Cheng JG, *et al*. High temperature transport and thermoelectric properties of Ag-substituted $Ca_3Co_4O_{9+\delta}$ system. *J Alloys Compd* 2008, **448**: 1–5.

[12] Ye JQ, Li HD, He QL. Thermoelectric properties of $Bi_{1.5}Pb_{0.5}Sr_{2-x}La_xCo_2O_y$ polycrystalline materials. *Rare Met* 2011, **30**: 501–504.

[13] Wang HC, Wang CL, Su WB, *et al*. Doping effect of La and Dy on the thermoelectric properties of $SrTiO_3$. *J Am Ceram Soc* 2011, **94**: 838–842.

[14] Xu G. High-temperature transport properties of Nb and Ta substituted $CaMnO_3$ system. *Solid State Ionics* 2004, **171**: 147–151.

[15] Snyder GJ, Toberer ES. Complex thermoelectric materials. *Nat Mater* 2008, **7**: 105–114.

[16] Popuri SR, Decourt R, McNulty JA, *et al*. Phonon–glass and heterogeneous electrical transport in A-site-deficient $SrTiO_3$. *J Phys Chem C* 2019, **123**: 5198–5208.

[17] Wang J, Zhang BY, Kang HJ, *et al*. Record high thermoelectric performance in bulk $SrTiO_3$ via nano-scale modulation doping. *Nano Energy* 2017, **35**: 387–395.

[18] Dylla MT, Kuo JJ, Witting I, *et al*. Grain boundary engineering nanostructured $SrTiO_3$ for thermoelectric applications. *Adv Mater Interfaces* 2019, **6**: 1900222.

[19] Wu C, Li J, Fan YC, *et al*. The effect of reduced graphene oxide on microstructure and thermoelectric properties of Nb-doped A-site-deficient $SrTiO_3$ ceramics. *J Alloys Compd* 2019, **786**: 884–893.

[20] Okhay O, Zlotnik S, Xie WJ, *et al*. Thermoelectric performance of Nb-doped $SrTiO_3$ enhanced by reduced graphene oxide and Sr deficiency cooperation. *Carbon* 2019, **143**: 215–222.

[21] Rost CM, Sachet E, Borman T, *et al*. Entropy-stabilized oxides. *Nat Commun* 2015, **6**: 8485.

[22] Liu J, Shao G, Liu D, *et al*. Design and synthesis of chemically complex ceramics from the perspective of entropy. *Mater Today Adv* 2020, **8**: 100114.

[23] Oses C, Toher C, Curtarolo S. High-entropy ceramics. *Nat Rev Mater* 2020, **5**: 295–309.

[24] Gild J, Samiee M, Braun JL, *et al*. High-entropy fluorite oxides. *J Eur Ceram Soc* 2018, **38**: 3578–3584.

[25] Zhao ZF, Xiang HM, Chen H, *et al*. High-entropy $(Nd_{0.2}Sm_{0.2}Eu_{0.2}Y_{0.2}Yb_{0.2})_4Al_2O_9$ with good high temperature stability, low thermal conductivity, and anisotropic thermal expansivity. *J Adv Ceram* 2020, **9**: 595–605.

[26] Tsai K-Y, Tsai M-H, Yeh J-W. Sluggish diffusion in Co–Cr–Fe–Mn–Ni high-entropy alloys. *Acta Mater* 2013, **61**: 4887–4897.

[27] Ye YF, Wang Q, Lu J, *et al.* High-entropy alloy: Challenges and prospects. *Mater Today* 2016, **19**: 349–362.

[28] Lee C, Song G, Gao MC, *et al*. Lattice distortion in a strong and ductile refractory high-entropy alloy. *Acta Mater* 2018, **160**: 158–172.

[29] Shibagaki S, Fukushima K. XPS analysis on Nb–$SrTiO_3$ thin films deposited with pulsed laser ablation technique. *J Eur Ceram Soc* 1999, **19**: 1423–1426.

[30] Popuri SR, Scott AJM, Downie RA, *et al*. Glass-like

thermal conductivity in $SrTiO_3$ thermoelectrics induced by A-site vacancies. *RSC Adv* 2014, **4**: 33720–33723.

[31] Ren GK, Lan JL, Ventura KJ, *et al*. Contribution of point defects and nano-grains to thermal transport behaviours of oxide-based thermoelectrics. *npj Comput Mater* 2016, **2**: 16023.

[32] Snyder GJ, Snyder AH, Wood M, *et al*. Weighted mobility. *Adv Mater* 2020, **32**: 2001537.

[33] Cutler M, Leavy JF, Fitzpatrick RL. Electronic transport in semimetallic cerium sulfide. *Phys Rev* 1964, **133**: a1143.